Equations and Numerical Schemes coded in DassFlow2D

Contributors: see DassFlow webpage[1]

[1]*Institut de Mathémathiques de Toulouse / INSA / CNRS / INRAe / ICUBE Strasbourg*

March 2022

Contents

1   Mathematical models & data assimilation features

DassFlow 2D is an open computational software designed to shallow free surface flows with features of Variational Data Assimilation. The dynamics flow model can be coupled with a hydrology model, therefore providing a complete hydraulic-hydrology model.

The computational kernel is coded in Fortran 2003 / MPI. It is wrapped in Python.
In the latest version, the following physical models are available: the 2D SW equations in variables (h, q_x, q_y), its version for Herschel-Bulkley rheology (non Newtonian fluids, power-law rheology with threshold) and the GR4H rainfall-rainoff model.

Note that a 1D version of SW system in variables (S, Q) (Saint-Venant's equations) is available but in another DassFlow version (please consult DassFlow webpage for details).

1.1   The 2D SW equations for Newtonian fluids

Let us denote by h the water depth (m), by $\mathbf{q}$ the discharge (m^3/s), $\mathbf{q} = h\mathbf{u}$, $\mathbf{u} = (u, v)^T$ the depth-averaged velocity (m/s).

On a computational domain $\Omega \in \mathbb{R}^2$ and for a time interval $[0, T]$, the equations numerically solved are:

$$\begin{cases} \partial_t h + div(\mathbf{q}) & = & 0 & \text{in} \quad \Omega \times]0, T] \\[2em] \partial_t \mathbf{q} + div\left(\dfrac{\mathbf{q} \otimes \mathbf{q}}{h} + g\dfrac{h^2}{2}Id\right) & +gh\nabla z_b & = -g\dfrac{n^2 \|\mathbf{q}\|}{h^{7/3}}\mathbf{q} & \text{in} \quad \Omega \times]0, T] \end{cases} \tag{1}$$

where g is the magnitude of the gravity, z_b the bed elevation and n the Manning-Strickler roughness coefficient.

It is accompanied by initial and all usual boundary conditions necessary for real-world applications.

In the sequel we denote by: $\mathbf{U} = (h, \boldsymbol{q}) = (h, h\boldsymbol{u}) = (h, q_x, q_y)$.

1.2   The 2D SW equations for Non-Newtonian fluids (Herschel-Bulkley rheology)

For non-Newtonian flows, the SW equations with Herschel-Bulkley rheology writes:

$$\begin{cases} \partial_t h + div(\mathbf{q}) & = & 0 & \text{in} \quad \Omega \times]0, T] \\[2em] \partial_t \mathbf{q} + div\left(\dfrac{\mathbf{q} \otimes \mathbf{q}}{h} + \frac{1}{2}gh^2\cos\theta\boldsymbol{I} + \xi h^{2m+3}\right) & = & -gh\left(\cos\theta\nabla z_b - S_\theta\right) - \frac{1}{\rho}K\boldsymbol{\tau}_b & \text{in} \quad \Omega \times]0, T] \end{cases} \tag{2}$$

where;

$$\xi = \left[\frac{1}{(2m+3)(m+2)^2}\left[\frac{\rho g}{K}S_\theta\right]^{2m}\right] \text{ and } S_\theta = \begin{cases} \sin\theta & \text{for flows with low viscosity} \\ \sin\theta - \cos\theta\nabla H & \text{for flows with relatively high viscosity} \end{cases}$$

$$K\boldsymbol{\tau}_b = \left[\tau_c + K\left[\frac{\boldsymbol{q}}{\left(h - \frac{\tau_c}{\rho g S_\theta}\right)\left(\frac{1}{m+1}h - \frac{1}{(m+1)(m+2)}\left[h - \frac{\tau_c}{\rho g S_\theta}\right]\right) + \left(\frac{\rho g S_\theta}{\rho g S_\theta h - \tau_c}\right)^m\left(\frac{z_b^{m+2}}{(m+1)(m+2)} + Ch^{m+1}\right)}\right]^{\frac{1}{m}}\right]$$

with;
$\tau_c = \rho g S_\theta h_p(z, t)$, $h_p(z, t) = h(z, t) - h_c(z, t)$ and $m = \frac{1}{n}$
where n denotes the power-law index, H the fluid elevation, τ_b the basal shear stress, $K(T)$ the consistency index which is temperature-dependent, τ_c the yield stress , h_c the thickness of the sheared zone , h_p the plug thickness, and C the basal slip coefficient.

Similarly, the usual initial and boundary conditions are imposed.

1.3   The bucket-type rainfall-runoff model

The GR4H model ([**?**]) is a lumped continuous model that runs at the hourly time step. It is based on the GR4J model formulation of [**?**] and uses a robust and parsimonious production function proposed in ([**?**]). It is a well-established, parsimonious and robust model and its state-space version ([**?**]) is based on Ordinary Differential Equations (ODEs) hence differentiable. This property is a necessary condition to generate an adjoint code.

Several GR models exist, featuring varying amounts of parameters, stores and time steps (see [**?**]). The "state-space" version of the GR4H model is described by the following set of ODEs equations:

$$\frac{\mathrm{d}\boldsymbol{h}}{\mathrm{dt}} = \begin{cases} \dot{h}_p & = P_s - E_s - P_{erc} \\ \dot{h}_1 & = P_r - Q_{Sh,1} \\ \dot{h}_2 & = Q_{Sh,1} - Q_{Sh,2} \\ ... & ... \\ \dot{h}_{nres} & = Q_{Sh,nres-1} - Q_{Sh,nres} \\ \dot{h}_r & = Q_9 + F - Q_r \end{cases} \tag{3}$$

It consists in a production store S, a routing store R and a series of 11 Nash cascade stores $S_{h,i}$, $\forall i \in [1..11]$. The internal model variables are the 13 store levels. Four parameters (x_1, x_2, x_3, x_4) rule the draining of the production store, of the routing store, of the 11 identical cascading stores and the non-conservative exchange law. Initial store states are given using a 1 year warm-up period.

They involve the following fluxes:

$$\begin{cases} E_s = & E\left(\frac{2h_S}{c_1} - \left(\frac{h_p}{c_1}\right)^\alpha\right) \\ P_S = & P\left(1 - \left(\frac{h_p}{c_1}\right)^\alpha\right) \\ P_{erc} = & \left(\frac{\nu}{c_1}\right)^{\beta-1} \frac{1}{\beta-1}\left(h_p^+\right)^\beta \\ P_R = & P\left(\frac{h_p}{c_1}\right)^\alpha + \left(\frac{\nu}{c_1}\right)^{\beta-1}\frac{1}{\beta-1}\left(h_p^+\right)^\beta \\ Q_{N1} = & \frac{n_{res}-1}{c_4}h_1^+ \\ ... & ... \\ Q_{N11} = & \frac{n_{res}-1}{c_4}h_{n_{res}}^+ \\ Q_9 = & \Phi\frac{n_{res}-1}{c_4}h_{n_{res}}^+ \\ Q_1 = & (1-\Phi)\frac{n_{res}-1}{c_4}h_{n_{res}}^+ \\ F = & \frac{c_2}{c_3^\omega}\left(h_r^+\right)^\omega \\ Q_D = & (1-\Phi)\frac{n_{res}-1}{c_4}h_{n_{res}+1} - \frac{c_2}{c_3^\omega}\left(h_r^+\right)^\omega \\ Q_R = & \frac{1}{\left(h_R^+\right)^{\gamma-1}(\gamma-1)}\left(h_r^+\right)^\gamma \end{cases} \tag{4}$$

The following parameter are set following [**?**] and [**?**]: $\alpha = 2$, $\beta = 5$, $\gamma = 5$, $\omega = 3.5$, $\nu = 4/9$, $\Phi = 0.9$, $n_{res} = 11$.

1.4 Data Assimilation & inversion capabilities

The cost functions to be minimized (defined from the direct model output) is defined by the user, in particular the cost terms measuring the discrepancy between the simulated state and data. Data can be provided by external datasets (e.g. in-situ or satellites datasets). For experiment purposes, datasets can be produced by the code itself (this is the twin experiments mode).

The inversions are minimization process requiring the cost function gradient. The latter is computed by the adjoint method. The adjoint code is generated by performing the Automatic Differentiation tool Tapenade [1]. The source code written in Fortran and Makefile(s) have been designed to do so.

The cost gradient computation enables to analyse spatially-distributed sensitivities: this the 'local sensitivity mode'.

A complete Variational Data Assimilation process is available. This provides a calibrated model from datasets and/or the identification of some input parameters values (e.g. the bathymetry, some inflows or physical parametrizations) . The VDA process is based on local minimization algorithms (generally the BFGS algorithm).

Both the direct code and the adjoint code can be runned in parallel (MPI).

2 Finite Volume schemes

In this section, we describe the numerical schemes based on Finite Volume methods to solve the 2D SW models.

2.1 Notations and fundamentals

We consider a discretization $\mathfrak{I}_h$ of a computational domain Ω with N cells K_i (cells can be triangles or quadri-laterals that can be also mixed in practice).

---

[1] http://www-sop.inria.fr/tropics/

Let us introduce some notations and conventions (see Fig.1). Considering a given cell K (omitting above i index),

- m_K is the area of the cell K, $m_{\partial K}$ its perimeter and x_K its barycenter.

- e is one of the δK boundary edges, m_e its length and x_e its center.

- K_e is the neighboring cell to K across e.

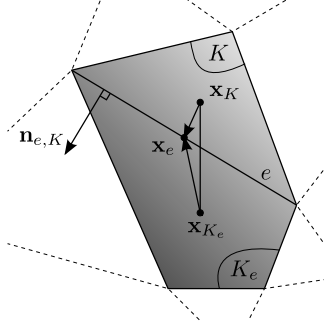- $\mathbf{n}_{e,K}$ is the unit normal to e oriented from K to K_e.

Figure 1: Notations and conventions for mesh discretization and numerical schemes associated.

The SW equations are written in their conservative form as follows:

$$\partial_t \mathbf{U} + \partial_x \mathbf{F}(\mathbf{U}) + \partial_y \mathbf{G}(\mathbf{U}) \;=\; \mathbf{S}_g(\mathbf{U}) + \mathbf{S}_f(\mathbf{U})$$

$$\mathbf{U} = \begin{bmatrix} h \\ hu \\ hv \end{bmatrix} \;,\; \mathbf{F}(\mathbf{U}) = \begin{bmatrix} hu \\ hu^2 + g\dfrac{h^2}{2} \\ huv \end{bmatrix} \;,\; \mathbf{G}(\mathbf{U}) = \begin{bmatrix} hv \\ huv \\ hv^2 + g\dfrac{h^2}{2} \end{bmatrix} \;,\tag{5}$$

$$\mathbf{S}_g(z_b; \mathbf{U}) = -g \begin{bmatrix} 0 \\ h\nabla z_b \end{bmatrix} \;,\; \mathbf{S}_f(\mathbf{U}) = -gn^2 \begin{bmatrix} 0 \\ \dfrac{\|\mathbf{u}\|}{h^{1/3}}\mathbf{u} \end{bmatrix}$$

The term $\mathbf{S}_g(z_b; \mathbf{U})$, resp. $\mathbf{S}_f(\mathbf{U})$, denotes the gravitational term, resp. the friction term.

The expression of $\mathbf{S}_f(\mathbf{U})$ above derives from the Manning-Strickler law, with n the Manning coefficient (friction coefficient). $n^2 = K_S^{-1}$, K_S the Strickler coefficient.

We consider the piecewise constant approximation over mesh cells:

$$\mathbf{U}_K = \frac{1}{m_K} \int_K \mathbf{U} dK \tag{6}$$

2.2 Schemes for the conservative fluxes

2.2.1 Basic principles

A each time step, the basic principle consists to solve first the hyperbolic system (5) *without* the source term $\mathbf{S}_f$, next to solve the dynamics system with this source term $\mathbf{S}_f$ only (i.e. $\partial_t \mathbf{U} = \mathbf{S}_f(\mathbf{U})$).

We consider a non uniform time grid: $t^{n+1} = t^n + \Delta t^n$. We denote by $\mathbf{U}_K^n$ (resp. by $\mathbf{U}_K^{n+1}$) the piecewise constant approximation of $\mathbf{U}$ at time t^n (resp. t^{n+1}). Recall that: $\mathbf{U} = (h, \boldsymbol{q}) = (h, h\boldsymbol{u}) = (h, q_x, q_y)$.

Let us consider here the hyperbolic system (5) *without* the source terms $\mathbf{S}_g(z_b; \mathbf{U})$ and $\mathbf{S}_f$:

$$\partial_t \mathbf{U} + \partial_x \mathbf{F}(\mathbf{U}) + \partial_y \mathbf{G}(\mathbf{U}) \;= 0 \tag{7}$$

The current cell ("left cell") is denoted by K. The "right cell" is denoted by K_e.

By integrating over K, and by applying the Godunov method [9], the semi-discrete scheme for the homogeneous system reads:

$$\mathbf{U}_K^{n+1} = \mathbf{U}_K^n - \frac{\Delta t^n}{m_K} \sum_{e \in \partial K} m_e \mathbf{F}_e \left(\mathbf{U}_K^n, \mathbf{U}_{K_e}^n, \mathbf{n}_K \right) \tag{8}$$

The rotational invariance property of the SW equations (5) allows to reduce this sum of 2D problem to a sum of 1D local Riemann problems such that: $\mathbf{F}_e \left(\mathbf{U}_K^n, \mathbf{U}_{K_e}^n, \mathbf{n}_K \right) = \mathbf{R}_K^{-1} \hat{\mathbf{F}}_e \left(\hat{\mathbf{U}}_K^n, \hat{\mathbf{U}}_{K_e}^n \right)$ with $\hat{\mathbf{U}}_K^n = \mathbf{R}_K \mathbf{U}_K^n$ where $\mathbf{R}_K$ is the rotation matrix, see e.g. [24].

Note that for a computational efficiency in the code, given an edge e, the fluxes are computed in both ways: from left to right and from right to left.

2.2.2 First order scheme

The HLLC approximate Riemann solver is used. We have, see e.g. [24] and references therein:

$$\left\{ \begin{array}{c} \left[\hat{\mathbf{F}}_e^{HLLC} \right]_{1,2} = \dfrac{s_{K_e} \left[\mathbf{F}(\hat{\mathbf{U}}_K) \right]_{1,2} - s_K \left[\mathbf{F}(\hat{\mathbf{U}}_{K_e}) \right]_{1,2} + s_K s_{K_e} \left(\left[\hat{\mathbf{U}}_{K_e} \right]_{1,2} - \left[\hat{\mathbf{U}}_K \right]_{1,2} \right)}{s_{K_e} - s_K} \\ \\ \left[\hat{\mathbf{F}}_e^{HLLC} \right]_3 = \left[\hat{\mathbf{F}}_e^{HLLC} \right]_1 \hat{v}* \quad \text{with} \quad \hat{v}* = \left\{ \begin{array}{ll} \hat{v}_K & \text{if} \quad s^* \geq 0 \\ \hat{v}_{K_e} & \text{if} \quad s^* < 0 \end{array} \right. \end{array} \right. \tag{9}$$

The wave speed expression are those proposed in [25]:

$$\begin{array}{l} s_K = \min \left(0, \hat{u}_K - \sqrt{gh_K}, \hat{u}_{K_e} - 2\sqrt{gh_{K_e}} + \sqrt{gh_K} \right) \\ s_{K_e} = \max \left(0, \hat{u}_{K_e} + \sqrt{gh_{K_e}}, \hat{u}_K + 2\sqrt{gh_K} - \sqrt{gh_{K_e}} \right) \end{array} \tag{10}$$

It has been demonstrated in in [25] that this insures L^∞ stability, positivity and consistency with entropy condition under a CFL condition.

For the intermediate wave speed estimate, following [24] we set:

$$s^* = \frac{s_K h_{K_e} \hat{u}_{K_e} - s_{K_e} h_K \hat{u}_K - s_K s_{K_e} (h_{K_e} - h_K)}{h_{K_e} (\hat{u}_{K_e} - s_{K_e}) - h_K (\hat{u}_K - s_K)} \tag{11}$$

The CFL-like condition for the time step Δt^n is, see e.g. [**?**]:

$$\Delta t^n = c \min_{K \in \Omega} \left(\frac{2\, m_K}{m_{\partial K} \left(\|\mathbf{u}_K^n\| + \sqrt{gh_K^n} \right)} \right) \tag{12}$$

with the constant $c \in [0.5, 0.8]$ in practice.

Note that it is usual to introduce a small cut-off water depth h_ϵ, if the velocity components vanishes in order to stabilize the numerical model or if round-off error generates a negative water depth. With the complete numerical scheme which is here developed, this cut-off can be set to a machine epsilon only.

The expressions above are next to be completed by the treatment of the source term S_f.

Well-balanced schemes with wet/dry front treatment

The numerical scheme must preserve the fluid at rest property, that is the gradient of bathymetry ∇z_b must not provide $\mathbf{u}^{n+1} \neq 0$ if $\mathbf{u}^n = 0$. In the presence of topography gradients (in particular those perpendicular to the streamlines) the basic topography gradient ∇z_b discretization in the gravity source term $\mathbf{S}_g(\mathbf{U})$ generates spurious velocities. There is no discrete balance between the hydrostatic pressure and the gravity source term anymore: $\nabla \left(gh^2/2 \right) \neq -gh\nabla z_b$.

The technique which is employed here is those presented in [2, 3]. It is based on the following change of variable.

From now, at left and right sides of edge e, the considered water depth values $h_\square^*$ are those defined from the "reconstructed" topography z_e as:

$$\begin{array}{l} h_\square^* = \max \left(0, h_\square + z_\square - z_e \right) \\ \text{with} \quad \left\{ \begin{array}{l} z_\square = \eta_\square - h_\square \\ z_e = \max \left(z_K, z_{K_e} \right) \end{array} \right. \end{array} \tag{13}$$

See Fig. 2.

The conservative variable vector $\mathbf{U}_{e,K}^n$ in the semi-discrete scheme (19) is now considered with the new variable:

$$\mathbf{U}_\Box^* = \begin{bmatrix} h_\Box^* \\ h_\Box^* \mathbf{u} \end{bmatrix} \tag{14}$$

Note that this new variable $h_{e,K}^*$ depends on the bathymetry values $z_{e,K}$ and z_e.
The resulting scheme reads:

$$\mathbf{U}_K^{n+1} = \mathbf{U}_K^n - \frac{\Delta t^n}{m_K} \sum_{e \in \partial K} m_e \left(\mathbf{F}_e(\mathbf{U}_K^{*n}, \mathbf{U}_{K_e}^{*n}, \mathbf{n}_K) + \mathbf{S}_p \left(\mathbf{U}_K^n, \mathbf{U}_K^{*n}; z_K, z_{K_e}, \mathbf{n}_K \right) \right) \tag{15}$$

with

$$\mathbf{S}_p \left(\mathbf{U}_K^n, \mathbf{U}_K^{*n}; z_K, z_{K_e}, \mathbf{n}_K \right) = \begin{bmatrix} 0 \\ \frac{g}{2} \left((h_K^n)^2 - (h_K^{n*})^2 \right) \mathbf{n}_K \end{bmatrix} \tag{16}$$

This provides a well-balanced (first order) scheme.

Figure 2: Typical situation of desired well-balanced property in presence of a wet/dry front. The WS elevation is here denoted by η.

2.2.3 Second order MUSCL scheme

We here develop a second order scheme based on the concepts of reconstruction and slope limiting initially introduced by Van Leer in the late 70's.

A monoslope second order Monotonic Upwind Scheme for Conservation Laws (MUSCL) scheme is adopted, see e.g. [5, 4]. This consists to "reconstruct" *locally linear fields by calculating a vectorial slope* $[\nabla \mathbf{U}_K^n]_i$ *in each cell K, for each variable i.*

The two "reconstructed" conservative variables vectors $\mathbf{U}_{\nabla,K}^n$ and $\mathbf{U}_{\nabla,K_e}^n$ at each side of edge e read as:

$$\mathbf{U}_{\nabla,\Box}^n = \mathbf{U}_\Box^n + \nabla \mathbf{U}_\Box^n . \overrightarrow{\mathbf{x}_\Box \mathbf{x}_\mathbf{e}} \tag{17}$$

with $\Box = K$ ("left cell") or K_e ("right cell"). For $\Box = K$, this reads:

$$\begin{bmatrix} h_{\nabla,K}^n \\ h_{\nabla,K}^n \mathbf{u}_{\nabla,K} \end{bmatrix} = \begin{bmatrix} h_K^n \\ h_K^n \mathbf{u}_K \end{bmatrix} + \begin{bmatrix} \nabla h_K^n \\ \nabla (h_K^n \mathbf{u}_K) \end{bmatrix} . \overrightarrow{\mathbf{x}_\Box \mathbf{x}_\mathbf{e}} \tag{18}$$

These two expressions replace $\mathbf{U}_K^n$ and $\mathbf{U}_{K_e}^n$ in the original first order semi-discrete scheme (8) to evaluate the numerical flux $\mathbf{F}_e$.

From these enriched linear conservative variable, the uncomplete basic FV scheme reads strictly the same:

$$\mathbf{U}_K^{n+1} = \mathbf{U}_K^n - \frac{\Delta t^n}{m_K} \sum_{e \in \partial K} m_e \mathbf{F}_e \left(\mathbf{U}_{\nabla,K}^n, \mathbf{U}_{\nabla,K_e}^n, \mathbf{n}_K \right) \tag{19}$$

Computation of the vectorial slopes With a such linear reconstruction, one can expect a scheme with a second-order accuracy in space (for regular solutions only). To this end, a least square method is employed to compute the vectorial slopes for each *primitive* variable denoted by $\mathbf{W}$.

$$\mathbf{W} = [h, u, v]^T \tag{20}$$

Let us defined the sum of squares for each i, $i = 1, \dots, 3$:

$$E_i\left(\left[\widehat{\nabla \mathbf{W}_K^n}\right]_i\right) = \sum_{e\in\partial K}\left([\mathbf{W}_{K_e}^n]_i - ([\mathbf{W}_K^n]_i + [\nabla \mathbf{W}_K^n]_i . \overrightarrow{\mathbf{x}_K \mathbf{x}_{K_e}})\right)^2 \tag{21}$$

Each term $E_i\left(\left[\widehat{\nabla \mathbf{W}_K^n}\right]_i\right)$ is minimized (as the solution of simple 2×2 linear systems).

This method represents a good alternative among others to find the hyperplane [5, 11] because of its accuracy and robustness independently to the number of neighbours. This is an important property as it will be shown later with the present wet/dry front treatment.

Limitation of the vectorial slopes   In order to prevent large numerical instabilities, the computed vectorial slopes above need to be limited.

Maximum Principle (MP) limiter

A first method consists to apply the Maximum Principle (MP) to the two edge (unlimited) reconstructed primitive variables calculated from (17) and (21).

Then the limited reconstructed variables $\mathbf{W}_{\nabla,K}^n$ and $\mathbf{W}_{\nabla,K_e}^n$ are defined as:

$$\min\left(\mathbf{W}_K^n, \mathbf{W}_{K_e}^n\right) \leq \mathbf{W}_{\nabla,K}^n \text{ and } \mathbf{W}_{\nabla,K_e}^n \leq \max\left(\mathbf{W}_K^n, \mathbf{W}_{K_e}^n\right) \tag{22}$$

This is the so-called the MP limiter.

In practice, this method generates moderate oscillations at solution singularities, whereas diffusion is minimized comparatively to other classic limiters like Minmod or Van Albada, see also e.g. [3, 17, 8, 7].

It is worth to point out that generation of new extremas in presence of wet/dry fronts can break the mass conservation, and in this case *the scheme is no longer positive.*

Well-balanced schemes with wet/dry front treatment

Following [2, 3], this issue is solved by evaluating the vectorial slope for the water surface elevation H rather than for the water height h. A new vectorial slope for the variable $\eta = h + z$ is first calculated in addition to the primitive variables ones.

As previously, the so-called hydrostatic reconstructed water depth $h_{e,K}^*$ is defined from the reconstructed topography z_e at edge e as:

$$h_{\nabla,\square}^* = \max\left(0, h_{\nabla,\square} + z_{\square} - z_e\right) \\ \text{with } \begin{cases} z_{\square} = \eta_{\square} - h_{\nabla,\square} \\ z_e = \max\left(z_K, z_{K_e}\right) \end{cases} \tag{23}$$

with $\square = K$ ("left cell") or K_e ("right cell"). See Fig. 2.

The conservative variable vector $\mathbf{U}_K^n$ in the semi-discrete scheme (19) is now considered with the new variable:

$$\mathbf{U}_{\nabla,\square}^* = \begin{bmatrix} h_{\nabla,\square}^* \\ (h^*\mathbf{u})_{\nabla,\square} \end{bmatrix} \tag{24}$$

Let us write the *second order scheme in space only* while considering the basic explicit Euler time scheme for sake of clarity. This reads:

$$\mathbf{U}_K^{n+1} = \mathbf{U}_K^n - \frac{\Delta t^n}{m_K} \sum_{e \in \partial K} m_e \mathbf{L}_e \left(\mathbf{U}_K^n, \mathbf{U}_{\nabla,K}^n, \mathbf{U}_{\nabla,K}^{*n}; \mathbf{U}_{\nabla,K_e}^{*n}; z_K, z_{K_e}, \mathbf{n}_K \right) \tag{25}$$

$$\mathbf{L}_e \equiv \mathbf{L}_e \left(\mathbf{U}_K^n, \mathbf{U}_{\nabla,K}^n, \mathbf{U}_{\nabla,K}^{*n}; \mathbf{U}_{\nabla,K_e}^{*n}; z_K, z_{K_e}, \mathbf{n}_K \right) = \mathbf{F}_e \left(\mathbf{U}_{\nabla,K}^{*n}; \mathbf{U}_{\nabla,K_e}^{*n}; \mathbf{n}_K \right) + \mathbf{S}_p \left(\mathbf{U}_{\nabla,K}^n, \mathbf{U}_{\nabla,K}^{*n}; z_K, z_{K_e}, \mathbf{n}_K \right) + \mathbf{S}_g \left(\mathbf{U}_K^n, \mathbf{U}_{\nabla,K}^n \right.$$
$$\tag{26}$$

with

$$\mathbf{S}_p \left(\mathbf{U}_{\nabla,K}^n, \mathbf{U}_{\nabla,K}^{*n}; z_K, z_{K_e}, \mathbf{n}_K \right) = \begin{bmatrix} 0 \\ \frac{g}{2} \left(\left(h_{\nabla,K}^n \right)^2 - \left(h_K^{n*} \right)^2 \right) \mathbf{n}_K \end{bmatrix} \tag{27}$$

and the gravitational uncentered corrective term:

$$\mathbf{S}_g \left(\mathbf{U}_K^n, \mathbf{U}_{\nabla,K}^n; z_K, \mathbf{n}_K \right) = \begin{bmatrix} 0 \\ \frac{g}{2} \left(h_{\nabla,K}^n + h_K^n \right) \left(z_{\nabla,K} - z_K \right) \mathbf{n}_K \end{bmatrix} \tag{28}$$

However, numerical experiments show that this scheme is not stable at wet/dry fronts perpendicular to the flow streamlines.

2.3   Splitting and friction source term

The friction source term is taken into account in the complete SW system by deriving a splitting method. This may be viewed as prediction-correction time scheme too. We refer to [24] Chapter 12.

We denote here by $\bar{\mathbf{U}}_K^{n+1}$ the FV solution at time t^{n+1} of the (well-balanced) scheme, either first or second order, of the SW system with the gravitational term $\mathbf{S}_g$ but without the friction term $\mathbf{S}_f$.

The notation $\bar{}$ should not be mixed up with depth-averaging...

Recall that we denote: $\mathbf{U} = (h, h\boldsymbol{u})^T$.

Prediction- correction scheme / splitting scheme

At each time step, from n to $n + 1$,

- **Step 1:** computation of $\bar{\mathbf{U}}^{n+1}$, solution of the conservative SW system, i.e. the SW system *without S_f,* i.e. the FV solution of the following system:

$$\partial_t \boldsymbol{U} + \partial_x \boldsymbol{F} \left(\boldsymbol{U} \right) + \partial_y \boldsymbol{G} \left(\boldsymbol{U} \right) = \mathbf{S}_g \left(\boldsymbol{U} \right) \tag{29}$$

Recall that the discrete form of Eq. 29 reads: for all K,

First order case:

$$\bar{\mathbf{U}}_K^{n+1} = \mathbf{U}_K^n - \Delta t^n \left[\frac{1}{m_K} \sum_{e \in \partial K} m_e \left(\mathbf{F}_e (\mathbf{U}_K^{*n}, \mathbf{U}_{K_e}^{*n}, \mathbf{n}_K) + \mathbf{S}_p \left(\mathbf{U}_K^n, \mathbf{U}_K^{*n}; z_K, z_{K_e}, \mathbf{n}_K \right) \right) \right] \tag{30}$$

Second order case:

$$\bar{\mathbf{U}}_K^{n+1} = \mathbf{U}_K^n - \Delta t^n \left[\frac{1}{m_K} \sum_{e \in \partial K} m_e \left(\mathbf{F}_e \left(\mathbf{U}_{\nabla,K}^{*n}; \mathbf{U}_{\nabla,K_e}^{*n}; \mathbf{n}_K \right) + \mathbf{S}_p \left(\mathbf{U}_{\nabla,K}^n, \mathbf{U}_{\nabla,K}^{*n}; z_K, z_{K_e}, \mathbf{n}_K \right) + \mathbf{S}_g \left(\mathbf{U}_K^n, \mathbf{U}_{\nabla,K}^n, z_K, \mathbf{n}_K \right) \right) \right]$$
$$\tag{31}$$

- **Step 2:** given the "predicted value" $\bar{\mathbf{U}}^{n+1}$, compute $\mathbf{U}^{n+1}$ solution of:

$$\partial_t \mathbf{U} = \mathbf{S}_f \left(\mathbf{U} \right) \tag{32}$$

Expression of $\mathbf{U}^{n+1}$ in the first order case

General schemes (explicit, implicit or semi-implicit ones) including the friction source term $\mathbf{S}_f$ in the discretization of the model (Eq. 5) can be written as: for all K,

$$\mathbf{U}_K^{n+1} = \bar{\mathbf{U}}_K^{n+1} + \Delta_t^n \mathbf{S}_f \left(\bar{\mathbf{U}}_K^{n+1}, \bar{\mathbf{U}}_{K_e}^{n+1} \right) \tag{33}$$

Note that this splitting scheme is consistent at first order in Δt with the complete SWE. Splitting scheme second order in time is possible; it is not detailed later.

In the case of the Manning-Strickler law, the friction term reads: $\mathbf{S}_f = -gn^2 \begin{bmatrix} 0 \\ \frac{|\bar{\boldsymbol{u}}|}{h^{\frac{1}{3}}} \bar{\boldsymbol{u}} \end{bmatrix}$.

Therefore the equation to be solved (Eq. 32) reads:

$$\partial_t \begin{pmatrix} h \\ h\bar{\boldsymbol{u}} \end{pmatrix} = -gn^2 \begin{pmatrix} 0 \\ \frac{|\bar{\boldsymbol{u}}|}{h^{\frac{1}{3}}} \bar{\boldsymbol{u}} \end{pmatrix} \tag{34}$$

Since the friction source term $\mathbf{S}_f$ is zero in the mass conservation equation, we remark that $h^{n+1} = \bar{h}^{n+1}$. As a consequence, we consider the non-zero momentum component only:

$$\partial_t (h\bar{\boldsymbol{u}}) = -gn^2 \frac{|\bar{\boldsymbol{u}}|}{h^{\frac{1}{3}}} \bar{\boldsymbol{u}} \tag{35}$$

Let us consider *the implicit scheme* (implicit in u and h):

$$\frac{h^{n+1}\boldsymbol{u}^{n+1} - h^{n+1}\bar{\boldsymbol{u}}^{n+1}}{\Delta t^n} = -gn^2 \frac{\left|\boldsymbol{u}^{n+1}\right| \boldsymbol{u}^{n+1}}{(h^{n+1})^{\frac{1}{3}}} \tag{36}$$

This implies that:

$$\left|\boldsymbol{u}^{n+1}\right| \boldsymbol{u}^{n+1} + \frac{(h^{n+1})^{\frac{4}{3}}}{\Delta t^n gn^2} \left(\boldsymbol{u}^{n+1} - \bar{\boldsymbol{u}}^{n+1} \right) = 0 \tag{37}$$

Let us set $c = \frac{(h^{n+1})^{\frac{4}{3}}}{\Delta t^n gn^2}$. $c \geq 0$.

Note that $\left|\boldsymbol{u}^{n+1}\right| \boldsymbol{u}^{n+1} + c\boldsymbol{u}^{n+1} = c\bar{\boldsymbol{u}}^{n+1}$. Therefore for non vanishing velocities, it exists $\alpha \in \,]0,1]$ such that: $\boldsymbol{u}^{n+1} = \alpha\bar{\boldsymbol{u}}^{n+1}$.

Adopting these notations, we obtain: $\left|\bar{\boldsymbol{u}}^{n+1}\right| \bar{\boldsymbol{u}}^{n+1} \alpha^2 + c\bar{\boldsymbol{u}}^{n+1}\alpha - c\bar{\boldsymbol{u}}^{n+1} = 0$. This simplifies to:

$$\left|\bar{\boldsymbol{u}}^{n+1}\right| \alpha^2 + c\,\alpha - c = 0 \tag{38}$$

Since $\alpha \geq 0$, the root of this quadratic equation reads:

$$\alpha = \frac{-c + \sqrt{c^2 + 4c\left|\bar{\boldsymbol{u}}^{n+1}\right|}}{2\left|\bar{\boldsymbol{u}}^{n+1}\right|} \tag{39}$$

Let us define the function $\varepsilon = \frac{1}{c}\left|\bar{\mathbf{u}}^{n+1}\right| = \Delta t^n gn^2 \frac{|\bar{\mathbf{u}}^{n+1}|}{(h^{n+1})^{4/3}}$.

Observe that $\varepsilon = O(\Delta t^n)$, also $\varepsilon = O\left(\frac{|\bar{\mathbf{u}}^{n+1}|}{(h^{n+1})^{4/3}}\right)$.

By adopting this notation, the expression (39) of α reads: $\alpha = \frac{\sqrt{1+4\epsilon}-1}{2\epsilon}$.

After some rearrangements, we obtain:

$$\alpha = \frac{2}{1 + \sqrt{1 + 4\varepsilon}} \tag{40}$$

At 1st order in ϵ, we get: $\alpha \sim \left(\frac{1}{1+\epsilon/4}\right) \sim 1 - \epsilon/4$.

Finally, we obtain:

$$\boldsymbol{u}^{n+1} = \left(\frac{2(h^{n+1})^{2/3}}{(h^{n+1})^{2/3} + \sqrt{(h^{n+1})^{\frac{4}{3}} + 4\Delta t^n gn^2 |\bar{\mathbf{u}}^{n+1}|}} \right) \bar{\boldsymbol{u}}^{n+1} \tag{41}$$

The final expression of the first order scheme is:

$$\mathbf{U}_K^{n+1} = \begin{pmatrix} h^{n+1} \\ h^{n+1}\boldsymbol{u}^{n+1} \end{pmatrix} = \left[\begin{array}{c} \bar{h}^{n+1} \\ h^{n+1}\bar{\mathbf{u}}^{n+1}\left(\dfrac{2\left(\bar{h}^{n+1}\right)^{2/3}}{\left(\bar{h}^{n+1}\right)^{2/3} + \sqrt{\left(\bar{h}^{n+1}\right)^{\frac{4}{3}} + 4\Delta t^n g n^2 \left|\bar{\mathbf{u}}^{n+1}\right|}} \right) \end{array} \right] \quad (42)$$

With $\left|\bar{\mathbf{u}}^{n+1}\right|$ the solution of Eq. 30 .

This is the first order scheme implemented into the code.

Note that the friction coefficient n may depend on the depth h like e.g. $n \equiv n(\alpha, \beta; h) = \alpha h^\beta$.

Expression of $\mathbf{U}^{n+1}$ in the second order case

In order to obtain a globally second order scheme, a higher-order time stepping scheme is needed.

A first possibility would be to replace the explicit splitted step for $\mathbf{S}_f$ in the classical second order SSP-RK2 method, see e.g. [10].

This time splitting strategy is stable and preserves positivity, however it is first order only !...

In order to derive an *actual second order scheme* with an full implicit discretization of the source term, Pareschi and Russo in [18] derive an IMplicit-EXplicit (IMEX) Runge-Kutta method for hyperbolic conservation laws with stiff relaxation terms.

Here we consider the scheme named IMEX-SSP(3,2,2). This provides the following scheme:

$$\begin{array}{rclcl} \mathbf{U}_K^{(1)} &=& \mathbf{U}_K^n & +\dfrac{\Delta t^n}{2}\mathbf{S}_f(\mathbf{U}_K^{(1)}, \mathbf{U}_K^n) \\ \mathbf{U}_K^{(2)} &=& 2\mathbf{U}_K^n - \mathbf{U}_K^{(1)} & +\dfrac{\Delta t^n}{2}\mathbf{S}_f(\mathbf{U}_K^{(2)}, \mathbf{U}_K^n) \\ \mathbf{U}_K^{(3)} &=& \mathbf{U}_K^n & +\Delta t^n \mathbf{L}_e(\mathbf{U}_K^{(2)}) \\ \mathbf{U}_K^{(4)} &=& \mathbf{U}_K^{(1)} + \mathbf{U}_K^{(2)} + \mathbf{U}_K^{(3)} - 2\mathbf{U}_K^n & +\dfrac{\Delta t^n}{2}\mathbf{S}_f(\mathbf{U}_K^{(4)}, \mathbf{U}_K^n) \\ \mathbf{U}_K^{(5)} &=& \mathbf{U}_K^n & +\Delta t^n \mathbf{L}_e(\mathbf{U}_K^{(4)}) \\ \mathbf{U}_K^{n+1} &=& \dfrac{1}{2}\left(\mathbf{U}_K^{(5)} - \mathbf{U}_K^{(3)}\right) + \mathbf{U}_K^{(4)} & \end{array} \quad (43)$$

with $\mathbf{L}_e(\mathbf{U}_K^{(l)}) \equiv \mathbf{L}_e\left(\mathbf{U}_K^{(l)}, \mathbf{U}_{\nabla,K}^{(l)}, \mathbf{U}_{\nabla,K}^{*(l)}; \mathbf{U}_{\nabla,K_e}^{*(l)}; z_K, z_{K_e}, \mathbf{n}_K\right)$ defined by (26).

The three stages implicit part of this time splitting is a DIRK scheme [18] respecting A-stability, L-stability. It is stiffly accurate ($R(\infty) = 0$) , see [12]. Such stability properties enable to deal with wet/dry fronts where the friction source term $\mathbf{S}_f$ is extremely stiff. ($\mathbf{S}_f$ stiff because the water depth vanishes).

Moreover this version of the DIRK scheme has been found important to treat non trivial boundaries conditions without any special correction.

This is the second order scheme implemented into the code.

2.4 Boundary conditions

Recall that the current cell is denoted by K ("left cell"). It is here a in-domain cell. Here K_e denotes the ghost cell ("right cell").

The basic idea to impose the boundary conditions is to define ghost conservative vectors: $\mathbf{U}_{K_e}^G$ for the first order scheme and $\mathbf{U}_{\nabla,K_e}^G$ for the second order for an edge e at the boundary of Ω.

Note that it is not straightforward to impose a numerical flux value e.g. $Q_{in}(t)$.

Let $\mathbf{U}_{K_e}^G$ be the value of $\mathbf{U}$ in a virtual (ghost) cell K_e adjacent to the boundary $\partial\Omega$.

Wall B.C. The following local Riemann problems are solved:

$$\begin{cases} h_{K_e}^G &=& h_K + (z_K - z_{K_e}) \\ \hat{u}_{K_e}^G &=& -\hat{u_K} \\ \hat{v}_{K_e}^G &=& \hat{v}_K \end{cases} \quad (44)$$

Imposed discharge: inflow discharge or rating curve at outflow To impose Q_{in} at Γ_{in} or a rating curve $Q_{out}(\eta)$ at Γ_{out}, whatever the fluid rheology, the following primitive variables ghost values are set in the local Riemann solver:

$$\begin{cases} h_{K_e}^G &= h_K \\ \hat{u}_{K_e}^G &= \dfrac{Q_{\text{user}} h_K^{2/3}}{\displaystyle\sum_{e \in \Gamma_{\text{in}}} h_{e,K}^{5/3} m_e} \\ \hat{v}_{K_e}^G &= \hat{v}_K \end{cases} \tag{45}$$

Q_{user} denotes either a given hydrogram $Q_{in}(t)$ (m^3/s), or a rating curve $Q_{out}(\eta)$.

The latter may be linearly interpoled function from tabulated values.

If the wetted cross-section at the boundary is not rectangular, the computed discharge value in K is a-priori not equal to the imposed value Q_{in} !...

To overcome this issue, a feedback process is applied on the ghost bathymetry z_{K_e} as follows:

$$z_{K_e}^{\text{new}} = z_{K_e}^{\text{old}} + cst\left(\mathbf{F}_e(\mathbf{U}_K^n, \mathbf{U}_{K_e}^n; \mathbf{n}_{e,K}) - q_{K_e}^G\right) \tag{46}$$

where: $q_{K_e}^G = h_K u_{K_e}^G (m^2/s)$ and cst can be changed ($cst = 0.1$ by default).

This process correct the ghost bathymetry z_b^G at each time step to finally converge to a value implying that the mass flux $\mathbf{F}_e^h(\mathbf{U}_K^n, \mathbf{U}_{K_e}^n, \mathbf{n}_{e,K})$ is stricly equal to the imposed lineic discharge $\hat{q}_{K_e}^G$.

Depth imposed In order to control the depth value at a boundary e.g. at Γ_{out}, the following values are considered:

$$\begin{cases} h_{K_e}^G &= h_{\text{user}} \\ \hat{u}_{K_e}^G &= \hat{u}_K + 2\sqrt{g}\left(\sqrt{h_{user}} - \sqrt{h_K}\right) \\ \hat{v}_{K_e}^G &= \hat{v}_K \end{cases} \tag{47}$$

Second-order case In the case of the second-order scheme, one has the "reconstructed" variable $\mathbf{U}_{\nabla,K_e}^G$; $\mathbf{U}_{K_e}^G$ is first used in the least square method (21) to compute the vectorial slope in the interior cell K.

The conditions (44), (45) and (47) are then used a second time replacing $\mathbf{U}_K$ by $\mathbf{U}_{\nabla,K}$ to obtain $\mathbf{U}_{\nabla,K_e}^G$.

Finally, the hydrostatic reconstructed depth $h_{K_e}^{*;G}$ and $h_{\nabla,K_e}^{*;G}$ are calculated in the same way through equations (13) and (23) with $z_{\nabla,K_e}^G = z_{\nabla,K_e}$.

3 Validation

This section is dedicated to the validation of the numerical schemes implemented in the DassFlow software presenting several challenging and relevant test cases in context of hydraulic and environmenetal studies : dam break, channel and run-up problems with dynamic wet/dry fronts and considering non-linear friction. We will show the formally global second-order convergence in space and time of our SW numerical model with the Manning-Strickler friction source term as the robust treatment of wet/dry fronts.

In order to quantify the numerical errors, we define these relative error norms,

$$e_p(x) = \frac{\|x^{\text{num}} - x^{\text{exact}}\|_p}{\|x^{\text{exact}}\|_p} \quad, \quad e_p^T(x) = \frac{1}{T}\int_0^T e_p(x)\,dt$$

$$\|x\|_p = \left(\sum_{K \in \Omega} m_K |x_K|^p\right)^{1/p} \tag{48}$$

where x^{num} is the numerical solution with n cells of discretization and x^{exact} is the analytical solution of the test case or the converge reference solution when the analytical solution is not known (x_i^{exact} is properly numerically integrated with desired accuracy in sense of used Finite Volume schemes).

3.1 Water at rest

We consider in a box 1000 meter long a zero bed elevation, ramdomly perturbated cell by cell with a maximum amplitude of $1\ m$,

$$z_b = r \quad \text{with} \quad r \in [-1, 1] \tag{49}$$

If the simualtion is initialized with a water elevation of zero, i.e. $z_b + h = 0$, the resulting "lake" should stay at rest. After a simulation time of 3600 s, the results with different schemes are showed in the Fig.(3). The norms of the final velocities are given in the Tab.1.

	1°order	1°order / WB-A	2°order	2°order / MP limiter / WB-A / CFL 0.5	2°order/ MP limiter / WB-A / CFL 0.25	2°order/ Barth limiter / WB-A
$\|\mathbf{u}\|_\infty$	2.30	$1.04\ 10^{-13}$	2.23	$1.45\ 10^{-2}$	$9.66\ 10^{-14}$	$7.66\ 10^{-14}$
$\|\mathbf{u}\|_1$	1.14	$6.92\ 10^{-16}$	0.95	$1.95\ 10^{-5}$	$9.40\ 10^{-16}$	$6.97\ 10^{-16}$

Table 1: Water at rest test case, absolute infinity and L_1 norms of the final velocities.

Figure 3: Water at rest test case, final water depth and velocities; (up-left) first order scheme; (up-right) well-balanced first order scheme; (down-left) well-balanced second order scheme with the MP limiter and a CFL number of 0.5; (down-right) well-balanced second order scheme with the Barth limiter.

3.2   Parabolic bowl with linear friction

Analytical solutions of the nonlinear SW equations considering a linear friction and a parabolic bottom topography were derived by Sampson [19], following the work of Thacker [23], by considering a linear friction in replacement of Coriolis force. These solutions involve a flat surface oscillating motion with wet/dry fronts, decaying over time because of friction. It gives a very popular test for a SW numerical solver [3, 15, 20, 14, 13]. The solution is,

$$
\begin{aligned}
\eta(x,t) &= h_0 + \frac{a^2 B^2 e^{-\tau t}}{8g^2 h_0}\left(-s\tau \sin 2st + \left(\frac{\tau^2}{4}-s^2\right)\cos 2st\right) \\
&\quad - \frac{B^2 e^{-\tau t}}{4g} - \frac{e^{-\tau t/2}}{g}\left(Bs\cos st + \frac{\tau B}{2}\sin st\right)x
\end{aligned}
\tag{50}
$$

$$
u(x,t) = Be^{-\tau t/2}\sin st
$$

with $p = \sqrt{8gh_0}/a$ and $s = \sqrt{p^2-\tau^2}/2$ (and then valid if $p > \tau$). We choose two set of parameters,

$$
\text{set 1}\ \begin{cases} h_0 &=\ 10\ m \\ a &=\ 3000\ m \\ B &=\ 5\ m.s^{-1} \\ \tau &=\ 0.001\ s^{-1} \end{cases} \qquad
\text{set 2}\ \begin{cases} h_0 &=\ 1\ m \\ a &=\ 30\ m \\ B &=\ 1\ m.s^{-1} \\ \tau &=\ 0.2\ s^{-1} \end{cases}
\tag{51}
$$

The first one corresponding to the classic parameters chosen into litterature as in [15, 14]. The Fig.(4) shows the calculated relative error norms $e_1^T(h)$ with this first set of parameters using the MP limiter for the second order well-balanced scheme. One can observe the correct convergence behavior of all well-balance schemes and demonstrate that the moving wet-dry fronts are robustly captured (a cut-off water depth $h_\epsilon \in \left[10^{-4}, 10^{-8}\right]$ have been used for these simulations in order to find a linear convergence behavior in log-log scale). A rate of convergence of approximatively 1.5 is found for the second-order well-balance scheme with the hybrid SSP-RK2 time splitting as with the IMEX time splitting (It is found a relative error norm $e_1^T(h) \simeq 2.10^{-3}$ for $n = 100$ which is approximatively the same in [15]). This loss of second order accuracy is most probably due to the presence of the two moving wet/dry fronts introducing singularities in the solution. But a most interesting observation is that there is no major difference between the two time splitting strategy despite the fact that the hybrid RK2 is first order accurate and the IMEX second order accurate, except maybe for very fine meshes. This demonstrates that the spatial consistency error is greater than the time one despite the accuracy slopes difference. If simulations are performed now with the second set of paramaters (51), then it is obtained a significant difference between the two time splitting methods Fig.(4). After an asymptotic first order behavior for coarse meshes, the hybrid RK2 time splitting gives a rate of convergence of 1 and the IMEX time splitting maintains the same 1.5 rate of convergence obtained with the first classic set of parameters (51).
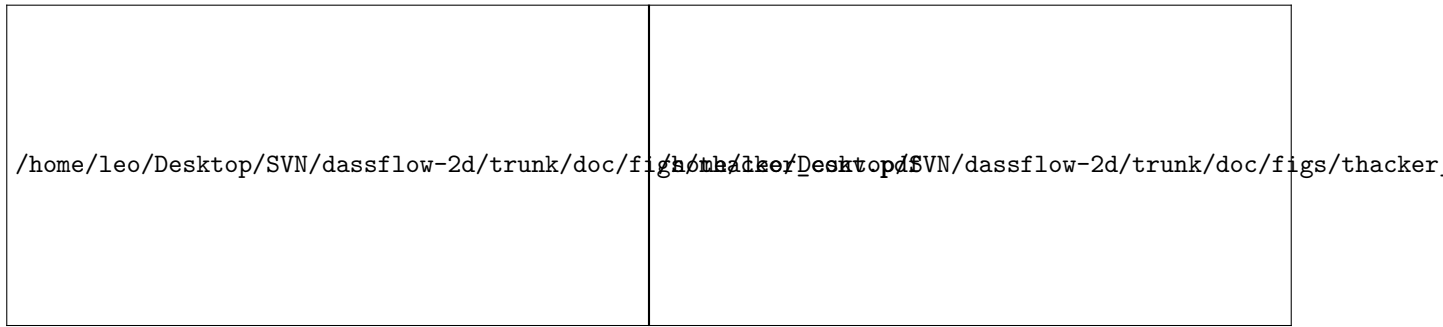
/home/leo/Desktop/SVN/dassflow-2d/trunk/doc/figs/thacker_	/home/leo/Desktop/SVN/dassflow-2d/trunk/doc/figs/thacker_

Figure 4: (left) Rate of convergence for the norm $e_1^T(h)$ with set 1 of physical parameters, n is the cells number (right) Same with set 2.

Nevertheless, the friction source term is linear for these simulations and it do not corresponds to our original model where the Manning-Strickler friction source term is non-linear. The singularities at the moving wet/dry fronts cannot guarantee to measure precisely the right accuracy of the numerical methods of regular solutions. In conclusion, this test case is interesting to check robustness to deal with wet/dry fronts, but largely insufficient to be relevant to test the behavior of our numerical solver in context of hydraulic and environnemental studies.

3.3   Dam break(s) with slope and non-linear friction

Numerical model behavior is investigated for dam break problems with a non zero slope and with the non-linear Manning-Strickler friction source term vanishing with the water depth at wet/dry front.

3.3.1   "Failling Gaussian"

A "regularised" dam break problem is first performed in sense that all eventual singularities in numerical solution are eliminated by construction. Considering the following initial condition,

$$
\begin{cases}
z_b(x) & = & 0.5 \quad e^{-\dfrac{(x - l_x/2)^2}{2 \, \sigma^2}} \\
h(x, t = 0) & = & 0.1 \; + \; 0.5 \quad e^{-\dfrac{(x - l_x/2)^2}{2 \, \sigma^2}}
\end{cases}
\tag{52}
$$

with $\sigma = 100 \; m$, a computational domain lenght $l_x = 1000 \; m$, a Manning-Strickler roughness coefficient $n = 0.05$ and a gravitational acceleration $g = 10 \; m.s^{-1}$, a converge simulation is performed with a 12800 cells mesh at time $t = 100 \; s$. Initial condition and converge result are plotted in Fig.5. One can note that these parameters are suitable in context of hydraulic. The topography gradient is chosen not constant in order to avoid an exact calculation of the topography gradient. The rates of convergence for the norms $e_1(h)$ and $e_1(q)$ showed on Fig.5 give a very clear accuracy result. As the hybrid RK2 time stepping method is only first order

accurate, the same overall first order convergence rate is found than for the spatial first order well-balanced scheme. The relative error norms are still smaller in significant proportion due to the enhanced spatial accuracy at second order. Concerning the IMEX time stepping method, a second-order rate of convergence is found. As a consequence, the relative error norms become very small even for very coarse meshes. This demonstrates the global second-order convergence rate of presented numerical model with MUSCL linear reconstruction with appropriate limitation and IMEX time stepping. Nevertheless, one may be careful that this rate of convergence will be smaller with singularities in numerical solution as with non trivial boundary conditions.
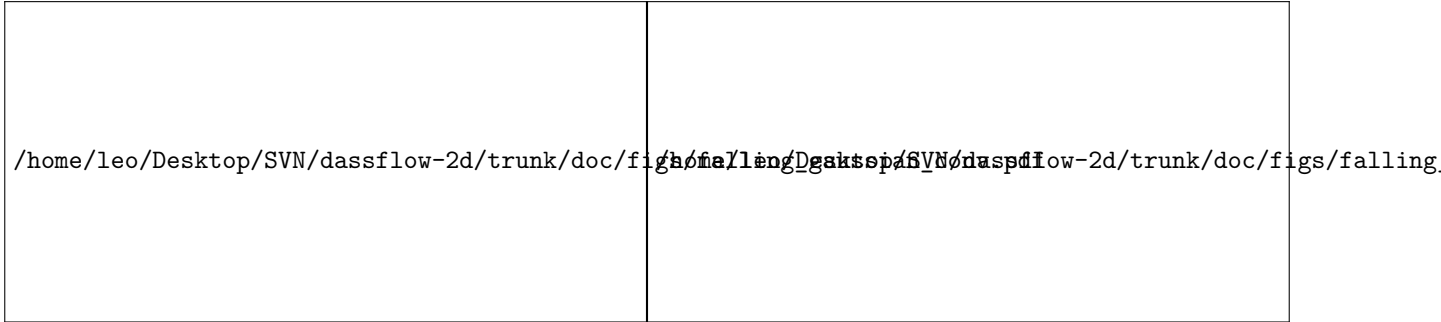
Figure 5: (left) Rates of convergence for the norms $e_1(h)$ and $e_1(q)$, n is the cells number (right) Half-domain initial condition, converge simulation with 12800 cells and relative simulations with 25 cells.

3.3.2 Flat slope and wet/dry front

The idealized dam break problem involving a dynamic wet/dry front is now investigated. The non-linear Manning-Strickler friction is taken into account and a non zero flat slope is considered as it is sketched in Fig.6. The parameters used are a computational domain length $l_x = 1000\ m$ with wall boundaries at each side, a slope $s = 0.5$ %, a Manning-Strickler roughness coefficient $n = 0.05$ and a gravitational acceleration $g = 10\ m.s^{-1}$. The water column has a length $L = 50\ m$ and two height are considered, $H = 1$ or $5\ m$.
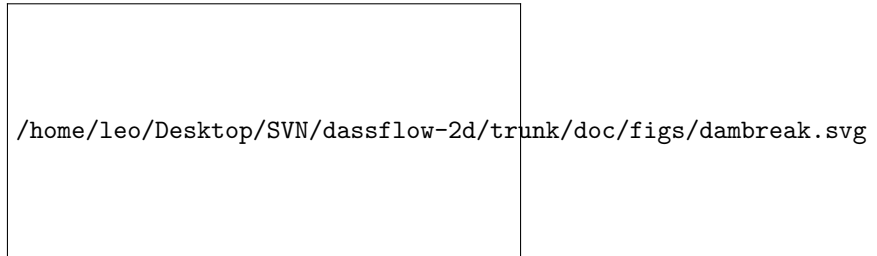

Figure 6: dam-break problem sketch.

As no analytical solution can be derived, two converge simulations are again performed with 12800 cells for $H = 5\ m$ at time $t = 500\ s$ and for $H = 1\ m$ at time $t = 2000\ s$. After the initial simulation time, a rarefaction wave goes upstream and interacts with the left wall boundary while a shock wave goes downstream, both modifing the initial water column shape. After a sufficient simulation time, the water column completly disappears and the new water shape exhibits more mass and stronger gradients downstream. The dynamic wet/dry front is robustly captured by well-balanced first- and second-order schemes without any cut-off water depth h_ϵ , despite that the well-balanced property is needless for this problem. We have verify that the schemes are stricly positive and do not generate any negative water depth.

Observing the relative error norms $e_1(h)$ in Fig.7 and Fig.8, on can first note that the previous obtained second-order convergence rate is loosed due to the singularities in the numerical solution and especially at

Figure 7: Idealized dam break problem with $H = 5\ m$. (left) rates of convergence for the norm $e_1(h)$ for different schemes; (right) corresponding initial condition, converge simulation with 12800 cells and results with 100 cells.
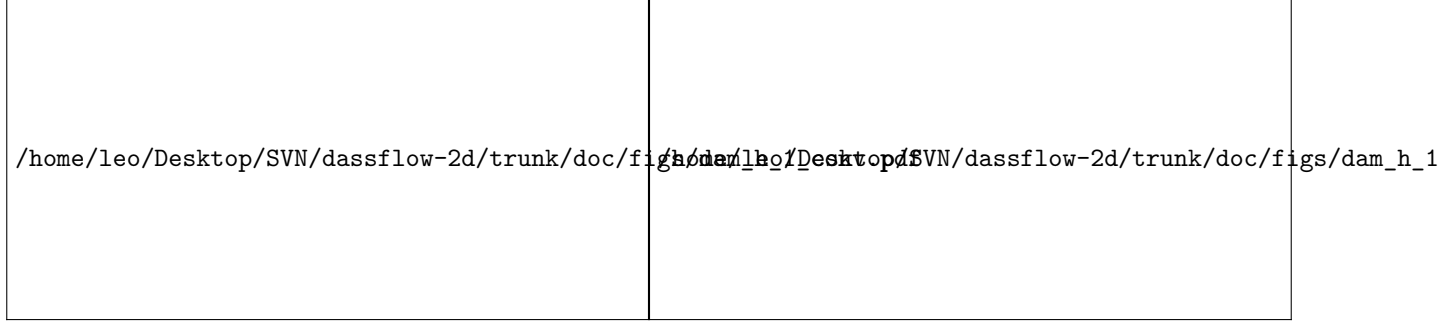

Figure 8: Idealized dam break problem with $H = 1\ m$. (left) rates of convergence for the norm $e_1(h)$ for different schemes; (right) corresponding initial condition, converge simulation with 12800 cells and results with 100 cells.

wet/dry front. Nevertheless, the relative error norm $e_1(h)$ is smaller for a given grid size using the IMEX time stepping rather than the hybrid RK2 one and even more comparatively to the first order schemes. If there is no major difference between the schemes with or without the well-balanced property when initially $H = 5\ m$, this difference is obvious when $H = 1\ m$. The well-balanced second-order scheme with the hybrid RK2 time stepping gives a result very similar to the first order scheme without the well-balanced property. This indicates a drawback in both well-balanced methods when the water depth is close to the bathymetry difference. Sufficiently important to give very wrong numerical solutions with first order schemes. In conclusion, in order to use these methods to simulate hydraulic flows, one may be careful to verify this criteria to produce meshes.

3.4 simple channel

In order to perform river flood simulations with real topography, it is interesting now to check the numerical model behavior to simulate an open-channel flow with a non constant topography gradient.

3.4.1 Mac Donald's benchmark

As it would be too restrictive to consider a channel with a constant topography gradient, the Mac Donald's analytic steady solution for open-channel flow is prefered [16]. Making the hypothesis of a contant discharge in space, it can be easily verify that the steady states verify,

$$\partial_t h = \partial_t q = \partial_x q = 0$$

$$\partial_x z_b = \left(\frac{q^2}{gh^3} - 1 \right) \partial_x h - \frac{n^2 q^2}{h^{10/3}} \tag{53}$$

that gives analytical steady solutions with a non necessary constant topography gradient. We consider like in [6] a computational domain lenght $l_x = 1000\ m$, a lineic discharge $q = 2\ m^2/s$ and a Manning-Strickler roughness coefficient $n = 0.033$. Considering this exact water depth,

$$h^{\text{exact}}(x) = \left(\frac{4}{g} \right)^{1/3} \left(1 + \frac{1}{2} \exp \left(-16 \left(\frac{x}{1000} - \frac{1}{2} \right)^2 \right) \right) \tag{54}$$

insuring that the flow is subcritical in all the channel, the bottom topography is numerically integrated with appropriate accurary that gives the xyplot Fig.9.
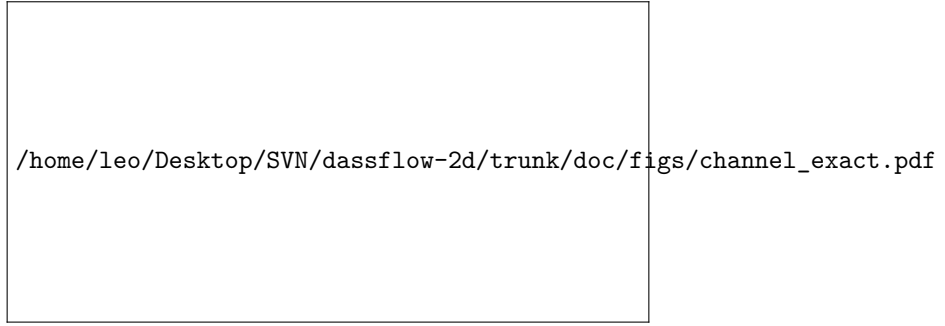
Figure 9: Open-channel steady state solution (53) considering the exact water depth (54).

The discharge is imposed upstream of the flow and the exact water depth is prescribed downstream. Initialising the simulations with dry cells except at the first cell at inflow, the steady states are properly achieved in time. The relative error norms $e_1(h)$ and $e_1(q)$ showed in Fig.10 give the same result than for the previous "regularised" dam break problem. The well-balanced second order scheme with the hybrid RK2 time stepping is only first order accurate with a smaller error than for the first order whereas with the IMEX time stepping the numerical model is formally at second order with very small errors even for very coarse meshes. A surprising result is that this rate of convergence is obtained with non trivial inflow/outflow boundary conditions even if this benchmark problem is only onedimensional.

Figure 10: Open-channel benchmark results : (left) relative error norms $e_1(h)$ and $e_1(q)$, n is the cells number; (right) exact solutions for h and u and simulations with 25 cells.

3.4.2 perturbed topography

The topography is not so smooth in real-life than in the previous test case where a channel 1000 m long was considered. It is tested here the numerical model introducing gradually in frequency some perturbations to an initial channel 10000 m long with a constant slope of $0,25$ % such that,

$$z_b = z_b + \sum_{i=1}^{n_p} 0.25 \sin\left(2\pi\left(\frac{p_i\,x}{l_x} + r_i\right)\right) \quad \text{with} \quad r_i \in [0,1] \tag{55}$$

with $n_p = 1, 2, 3, 4, 5$ and 6 and $p_i = 7, 24, 57, 108, 205$ and 402. In order to control the flow at inflow and outflow, and especially the backwater curve at the inflow, the topography gradient is kept constant close to taking care to maintain perturbations spatially continuous. The other parameters are a Manning-Strickler roughness coefficient $n = 0.05$, a lineic discharge $q = 1\ m^2/s$ and a gravitational acceleration $g = 10\ m.s^{-1}$. Since the exact solution for the initial constant slope channel is $h = 1\ m$ (and $u = 1\ m/s$), the topography perturbations are of the same order of magnitude. The opposite case would be obviously irrelevant. Main goal is to find a criteria that insures a good accuracy to apply the numerical model with real topography. Simulations are performed with the well-balanced second-order scheme and the IMEX time stepping until the steady state is properly found. For each of these six cases, a converge simulation is performed with 12800 cells of discretization showed at the left of the Fig.11. One can note that the flow respects the SW model hypothesis since the smaller wavelength has a value of 25 h.

/home/leo/Desktop/SVN/dassflow-2d/trunk/doc/figs/perturb_bathy_channel_slow.pdf	/home/leo/Desktop/SVN/dassflow-2d/trunk/doc/figs/perturb_

Figure 11: Channel 10000 m long with a constant slope of $0,25$ % introducing gradually in frequency some perturbations in topography according to (55) : (left) six cases with channel bottom topography and associated converge simulations; (right) associated relative error norm $e_1(h)$ with n cells of discretization (the greyer zone corresponds to less than 4 cells of discretization for the highest frequency for each case).

The calculation of the relative error norms $e_1(h)$ evolving the mesh step size n shows in Fig.11 that introducing gradually in frequency some perturbations in the topography damages the simulations accuracy. This phenomenom is in a first time likely proportional to the highest perturbation frequency before saturing when the mesh is too coarse comparatively to the highest frequency introduced. The criteria to maintain a good accuracy as the right correct second-order convergence rate is to discretize the channel topography with a minimum of four points for the highest perturbation frequency.

3.5   Solitary wave on a simple beach

It is well know that the SW equations can be a suitable model to study numerically storm surges as the complete life-cycle of a tsunami (generation, propagation and run-up on the coast). The classic benchmark problem was introduced by Synolakis and al. [22] deriving an adimensionnal analytical solution for the run-up of a solitary wave on a simple sloping beach. Following the parameters retained in the NOAA technical report for evaluation of tsunami numerical models [21], the initial condition with dimensional parameters sketched in Fig.12 is,

$$\eta(x,0) = H \ sech^2\left(\gamma\left(\frac{x - x_0 - L}{d}\right)\right) \quad \text{and} \quad u(x,0) = -\sqrt{\frac{g}{d}} \ \eta(x,0) \tag{56}$$

with $\cot\beta = 19.85$, $\gamma = \sqrt{3H/4d}$ and $L = \text{arccosh}\left(\sqrt{20}\right)/\gamma$. The wave height satifies the adimendional parameter $H/d = 0.0185$. The computational domain is $100\,d$ long, the mesh step size respects $\Delta x = d/10$ and wall boundaries conditions are prescribed. Using the well-balanced second-order numerical scheme with the MP limter and IMEX time stepping, resulting water levels profiles and two time series are plotted in Fig.13 as superposed the nonlinear analytical solution.
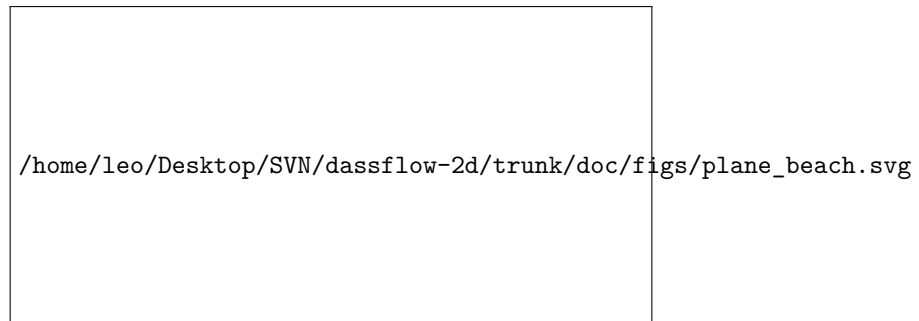
/home/leo/Desktop/SVN/dassflow-2d/trunk/doc/figs/plane_beach.svg

Figure 12: Dimensional sketch of the solitiary wave run-up benchmark problem sketch.

According to Synolakis and al. in [21] page 5, "*any well benchmarked code should produce results within 5% of the calculated value from the analytical solution*" which is the case for our simulation which is spatially

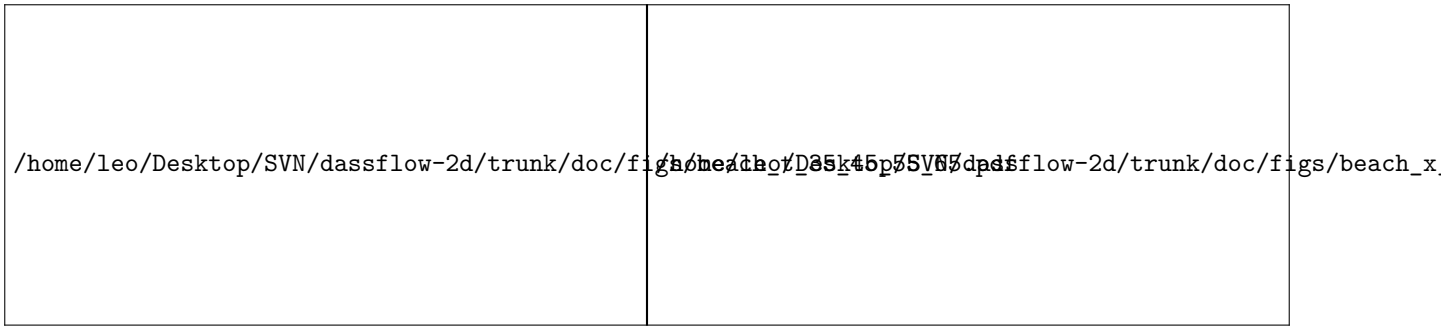|	
/home/leo/Desktop/SVN/dassflow-2d/trunk/doc/figs/beach_x_t35_45p5 SVN dassflow-2d/trunk/doc/figs/beach_x_	

Figure 13: Run-up of a solitiary wave on a simple beach : comparison of analytical solution (scatters) versus numerical solution (solid lines).

everywhere very close to the analytical solution. There is no particular "distortion" in the numerical solution at adimensional time $t/\tau = 45$ and 65 in proximity to the wet/dry front whereas other numerical models can produce some like it is showed in the NTHMP workshop report [1]. This demonstrates that our well-balanced treatment at wet/dry front do not affect a wave run-up computation accuracy.

References

[1] *Proceedings and results of the 2011 NTHMP model benchmarking workshop*, http://nthmp.tsunami.gov/index.html, 2012.

[2] E. Audusse, F. Bouchut, M.-O. Bristeau, R. Klein, and B. Perthame. A fast and stable well-balanced scheme with hydrostatic reconstruction for shallow water flows. *SIAM J. Sci. Comput.*, 25(6):2050–2065, June 2004.

[3] E. Audusse and M.-O. Bristeau. A well-balanced positivity preserving "second-order" scheme for shallow water flows on unstructured meshes. *J. Comput. Phys.*, 206(1):311–333, June 2005.

[4] T. Buffard and S. Clain. Monoslope and multislope muscl methods for unstructured meshes. *Journal of Comptutational Physics*, 229:3745–3776, 2010.

[5] P. Chévrier and H. Galley. A van leer finite volume scheme for the euler equations on unstructured meshes. *ESAIM: Mathematical Modelling and Numerical Analysis*, 27(2):183–201, 1993.

[6] C. Delestre, O.and Lucas, F. Ksinant, P.A.and Darboux, C. Laguerre, T.N.T. Vo, F. James, and S. Cordier. Swashes: a compilation of shallow water analytic solutions for hydraulic and environmental studies. 40 pages, April 2012.

[7] A. I. Delis and I. K. Nikolos. A novel multidimensional solution reconstruction and edge-based limiting procedure for unstructured cell-centered finite volumes with application to shallow water dynamics. *International Journal for Numerical Methods in Fluids*, 71(5):584–633, 2013.

[8] A.I. Delis, I.K. Nikolos, and M. Kazolea. Performance and comparison of cell-centered andÃÂ node-centered unstructured finite volume discretizations forÃÂ shallow water free surface flows. *Archives of Computational Methods in Engineering*, 18:57–118, 2011.

[9] S. K. Godunov. A difference method for numerical calculation of discontinuous solutions of the equations of hydrodynamics. *Math. Sbornik*, 47:271–306, 1959.

[10] S. Gottlieb, C.-W. Shu, and E. Tadmor. Strong stability-preserving high-order time discretization methods. *SIAM Rev*, 43:89–112, 2001.

[11] F. Haider, J.-P. Croisille, and B. Courbet. Stability analysis of the cell centered finite-volume muscl method on unstructured grids. *Numer. Math.*, 113(4):555–600, September 2009.

[12] E. Hairer and G. Wanner. *Solving Ordinary Differential Equations II: Stiff and Differential-Algebraic Problems.* Springer Series in Computational Mathematics. Springer, 2004.

[13] J. Hou, Q. Liang, F. Simons, and R. Hinkelmann. A 2d well-balanced shallow flow model for unstructured grids with novel slope source term treatment. *Advances in Water Resources*, 52(0):107 – 131, 2013.

[14] Q. Kesserwani, G.and Liang. Locally limited and fully conserved rkdg2 shallow water solutions with wetting and drying. *Journal of Scientific Computing*, 50:120–144, 2012.

[15] Q. Liang and F. Marche. Numerical resolution of well-balanced shallow water equations with complex source terms. *Advances in Water Resources*, 32(6):873–884, June 2009.

[16] I. MacDonald, M.J. Baines, N.K. Nichols, and P.G. Samuels. Analytic benchmark solutions for open-channel flows. *Journal of Hydraulic Engineering*, 123(11):1041–1045, 1997.

[17] I.K. Nikolos and A.I. Delis. An unstructured node-centered finite volume scheme for shallow water flows with wet/dry fronts over complex topography. *Computer Methods in Applied Mechanics and Engineering*, 198(47-48):3723–3750, 2009.

[18] L. Pareschi and G. Russo. Implicit-explicit runge-kutta schemes and applications to hyperbolic systems with relaxation. *Journal of Scientific Computing*, 25:129–155, 2005.

[19] J. Sampson, A. Easton, and M. Singh. Moving boundary shallow water flow above parabolic bottom topography. *ANZIAM Journal*, 47, 2006.

[20] L. Song, J. Zhou, J. Guo, Q. Zou, and Y. Liu. A robust well-balanced finite volume model for shallow water flows with wetting and drying over irregular terrain. *Advances in Water Resources*, 34(7):915–932, 2011.

[21] C. Synolakis. *Standards, criteria, and procedures for NOAA evaluation of tsunami numerical models*. NOAA evaluation of tsunami numerical models, 2007.

[22] C.E. Synolakis. The runup of solitary waves. *Journal of Fluid Mechanics*, 185:523–545, 1987.

[23] W.C. Thacker. Some exact solutions to the nonlinear shallow-water wave equations. *J. Fluid Mech.*, 107:499–508, 1981.

[24] E.F. Toro. *Shock-capturing methods for free-surface shallow flows*. John Wiley, 2001.

[25] J.-P. Vila. Simplified godunov schemes for 2 x 2 systems of conservation laws. *SIAM J. Numer. Anal.*, 23(6):1173–1192, December 1986.